



Constraining mornings & evenings on distant worlds: a new semi-analytical approach and prospects with transmission spectroscopy

NÉSTOR ESPINOZA ¹ AND KATHRYN JONES ²

¹*Space Telescope Science Institute, 3700 San Martin Drive, Baltimore, MD 21218, USA*

²*University of Bern, Center for Space and Habitability, Gesellschaftsstrasse 6, CH-3012, Bern, Switzerland*

(Received; Revised)

Submitted to AJ

ABSTRACT

The technique of transmission spectroscopy — the variation of the planetary radius with wavelength due to opacity sources in the planet’s terminator region — has been to date one of the most successful in the characterization of exoplanet atmospheres, providing key insights into the composition and structure of these distant worlds. One underlying assumption of the technique, however, is that the variations are the same in the entire terminator region. In reality, the morning and evening terminators might have distinct temperature, pressure and thus compositional profiles due to the inherent 3-D nature of the planet which would, in turn, give rise to different spectra on each side of it. Constraining those might be fundamental for our understanding of not only the weather patterns in these distant worlds, but also of planetary formation signatures which might only be possible to extract once these features are well understood. Motivated by this physical picture, in this work we perform a detailed study on the observational prospects of detecting this effect. We present an open-source semi-analytical framework with which this information can be extracted directly from transit lightcurves, and perform a detailed study on the prospects of detecting the effect with current missions such as *TESS* and upcoming ones such as *JWST*. Our results show that these missions show great promise for the detection of this effect. Transmission spectroscopy studies with *JWST*, in particular, could provide spectra of each of the limbs allowing us to convey 3-D information previously accessible only via phase-curves.

Keywords: editorials, notices — miscellaneous — catalogs — surveys

1. INTRODUCTION

The technique of transmission spectroscopy — the wavelength dependence of the planetary radius during transit (Seager & Sasselov 2000; Hubbard et al. 2001; Burrows et al. 2003; Fortney 2005), has been one of the most successful ones in the past decade to explore the composition and structure of exoplanet atmospheres, providing key insights into their interior structures and compositions (see, e.g., Kreidberg 2018, for a review). From an observational perspective, to obtain a transit spectrum researchers typically fit a transit model to precise wavelength-dependent light curves in order to re-

trieve the transit depths as a function of wavelength. To date, the modelling of these spectrophotometric light curves has relied in one simple, but key assumption: the terminator region we observe during transit is homogeneous. There is already growing evidence that this assumption might actually be unrealistic in relatively hot ($T_{\text{eq}} > 1000$) exoplanet atmospheres, where the day-to-night differences might in turn imply different structures and overall compositions in their morning and evening¹ terminators (see, e.g., Kempton et al. 2017; Powell et al. 2019; MacDonald et al. 2020; Helling et al. 2020, and references therein). Constraining them might give precious insights into circulation patterns and com-

Corresponding author: Néstor Espinoza
nespinoza@stsci.edu

¹ In this work, the morning and evening limbs are also referred to as the leading and trailing limbs, respectively.

positional stratification which might probe to be fundamental for our understanding of the weather patterns in distant worlds. For example, hazes are expected to be photochemically produced and thus they would most likely be able to form in the dayside (Kempton et al. 2017; Powell et al. 2019). These could, in turn, be transported to the trailing limb, while clouds could be transported from the nightside (where they are expected to form due to the lower temperatures) into the leading limb, thus resulting in a drastically different transmission spectrum between them, and thus effective sizes of the radii of each limb (Kempton et al. 2017; Powell et al. 2019). Directly detecting this effect would not only serve to put theories like the ones proposed by Kempton et al. (2017) and Powell et al. (2019) to the test, but would directly impact on the fundamental assumptions of transmission spectroscopy studies to date, implying there is not *one* set of properties (e.g., abundances) to extract from transmission spectra. This is, in turn, critical to perform inferences on e.g., formation scenarios based on extracted molecular abundances with this technique (see, e.g., Öberg et al. 2011; Mordasini et al. 2016; Espinoza et al. 2017, and references therein).

Previous works (e.g., Line & Parmentier 2016; Kempton et al. 2017; Powell et al. 2019; MacDonald et al. 2020) have already studied the prospects and impact of limb inhomogeneities on transit spectra. Overall, the consensus seems to be that there is already both observational and theoretical evidence that this is an effect that is important to consider and that might even be impacting current transit spectra. Line & Parmentier (2016), Kempton et al. (2017) and Powell et al. (2019) have already laid out the foundation of the theoretical aspects of detecting this effect. In this work, we explore these prospects from an observational perspective which aims at detecting the effect of limb asymmetries *directly in transit lightcurves*, such that interpretations (through, e.g., retrievals similar to those proposed in MacDonald et al. 2020) can be made at a later stage on each of the limbs. Although this proposition is not particularly new (it has already been suggested by the work of von Paris et al. 2016), our contribution in this work is to perform a deep dive into (a) *how* we might actually perform this characterization in a fast and reliable way, (b) *what is the level of detectability* of this effect with current and near-future instrumentation and (c) to show how, in some cases, this might even be *the most efficient way of extracting this information* from transit lightcurves. Some of these points have already been touched upon by Powell et al. (2019) at different degrees of depth; here we expand and homogenize the

discussion from an observational perspective, which we believe complements these previous works on this topic.

Our work is organized as follows. In Section 2 we present a new semi-analytical method to extract the transit depths from each of the limbs of an exoplanet. The core idea of this method was actually already put forward by von Paris et al. (2016), where each of the limbs of the exoplanet are modelled as stacked semi-circles. However, we expand on this modelling framework in that our calculation is made in a semi-analytical fashion, making use of geometrical arguments and the algorithm used by *batman* (Kreidberg 2015). This makes the lightcurve computation much faster than the numerical scheme described in von Paris et al. (2016), and allows to expand it to account for sky-projected *planetary* spin-orbit misalignments. We present a python library to generate lightcurves with this new algorithm, *catwoman* (Jones & Espinoza 2020), in Section 2.1, provide an overview of the model and validate it against a numerical implementation in Section 2.2. In Section 3 we present simulations in which we explore the feasibility of detecting this effect with current precise photometry such as that of the *Transiting Exoplanet Survey Satellite* mission (*TESS*; Ricker et al. 2014) and near-future instrumentation such as spectrophotometry to be obtained by the upcoming *James Webb Space Telescope* (*JWST*). In Section 4 we present a discussion and implications of our results, along with a case-study on the exoplanet HAT-P-41b, which we use to demonstrate how extracting the spectrum of the limbs of this exoplanet might give insights into possible models that give rise to the observed transit spectrum by the *Hubble Space Telescope* (*HST*). We summarize our main conclusions in Section 5.

2. MODELLING LIMB ASYMMETRIES IN TRANSIT LIGHTCURVES

The idea proposed by von Paris et al. (2016) to model the signatures of asymmetric limbs in transit lightcurves involves a very simple concept: approximate the terminator regions of the leading and trailing limbs as two stacked semi-circles with different radii. In essence, the idea is that each limb produces an independent transit spectrum that we ought to recover by modelling the lightcurve imprinted by them. In that work, the authors used a numerical framework to compute the resulting lightcurve, which is relatively computationally expensive. We here use the same idea but tackle the problem from a different angle: instead of using a numerical approach, we employ a semi-analytical framework, which in turn allows for faster lightcurve computations. In this new framework, the stacked semi-circles are also al-

lowed to be *rotated* with respect to the orbital motion, expanding thus the proposed framework by von Paris et al. (2016).

The basic problem we are trying to tackle is that of producing a transit lightcurve of two stacked semi-circles of (normalized, with respect to the stellar) radii $R_{p,1}$ and $R_{p,2}$ in front of their host star, where the semi-circles may be inclined with respect to the orbital motion by an angle φ . The geometrical configuration of the problem is depicted in Figure 1. We follow Kreidberg (2015) and assume a radially symmetric intensity profile $I(x)$, where $0 < x < 1$ is the normalized radial coordinate measured from the center of the star. With this, we can express the fraction of stellar light blocked by the object, δ , as (see Figure 1)

$$\delta = \sum_{i=1}^N I(x_m) \Delta A(x_m, R_{p,1}, R_{p,2}, \varphi, d), \quad (1)$$

where $x_m = (x_i + x_{i-1})/2$ is the middle point between x_i and x_{i-1} , and $\Delta A(x_m, R_{p,1}, R_{p,2}, \varphi, d)$ (for which we will refer in what follows simply as ΔA) is the intersectional area between the stacked semi-circles and the iso-intensity band depicted in Figure 1, where $R_{p,1}$ and $R_{p,2}$ are the radii of the semi-circles, φ is the rotation of the base of the semi-circles with respect to the orbital motion of the planet and d is the distance between the center of the star and the semi-circles. Because the form of $I(x_m)$ is usually known/parametrized via so-called limb-darkening laws, the challenge of finding the lightcurve of this configuration of stacked, rotated semi-circles is to find ΔA . The full derivation of this is presented in Appendix A; we present an overview of our implementation and validation of our approach below.

2.1. Implementation and model overview

Our semi-analytic approach to the problem has been implemented in the **catwoman** library (Jones & Espinoza 2020), which is fully documented² and available on Github³. In practice, **catwoman**’s code-base is that of **batman** Kreidberg (2015), and as such the library inherits most of the high-level functionalities of this latter library. A **catwoman** lightcurve, thus, receives as inputs the time-of-transit center t_0 , the period P of the orbit, the scaled semi-major axis a/R_* , the inclination i of the orbit with respect of the plane of the sky, the eccentricity e and argument of periastron ω of the orbit, and a set of limb-darkening coefficients for any of the laws already available in **batman**. On top of these, **catwoman** takes as

input the radii of each of the stacked semi-circles, $R_{p,1}$ and $R_{p,2}$, and the angle φ between the axis that connects them and the vector that follows the direction of motion in the orbit (see Figure 1).

The motivation behind allowing to define the angle φ in the lightcurve generation comes from the possibility of being able to detect the sky-projected spin-orbit misalignment of the *planet*, which is something the eclipse mapping technique for both lightcurves (Rauscher et al. 2007; Williams et al. 2006) and radial-velocities (Nikolov & Sainsbury-Martinez 2015) are able to do in principle. As will be shown in Section 3.3, detecting the effect of asymmetric lightcurves due to morning/evening terminator structural and/or compositional inhomogeneities almost guarantees the possibility of putting constraints on this angle, and ignorance on its value does not have a great impact on the detectability of the effect. One important point to consider on this parameter is that this defines the *instantaneous* angle between the axis that joins the semi-circles and the direction of the orbital motion (see Figure 1; orbital motion indicated with a dashed-line arrow). Because orbits as projected in the plane of the sky are curved in general, this means the axis that joins the semi-circles *rotates* when compared against a straight line projected in this plane. This effect has been implemented within **catwoman** as well (see Appendix A); we validate this implementation against a numerical implementation in the next sub-section.

2.2. Validation of the semi-analytical approach

In order to validate the semi-analytical approach presented here and implemented in the **catwoman** library, we built a numerical model that is also able to generate asymmetric lightcurves due to terminator inhomogeneities but through a completely independent and straightforward (albeit “brute-force”) approach. Our implementation of this numerical scheme is also available in Github⁴, and is detailed below.

Our approach of this numerical version of the lightcurve generation of asymmetrical transits is very similar to that of von Paris et al. (2016), and consists of simply discretizing the plane of the sky into $n_p \times n_p$ “pixels” centered around the target star. Pixels within the star are filled with values between 0 and 1 according to a given intensity profile $I(\mu)/I(1)$, while positions that include either the planet or the sky are filled with zeroes. The precision on the lightcurves generated by this scheme, thus, can be optimized by simply increasing n_p . In practice, this is implemented by populating a matrix

² <http://catwoman.readthedocs.io>

³ <https://github.com/KathrynJones1/catwoman>

⁴ https://github.com/nespinoza/numerical_catwoman

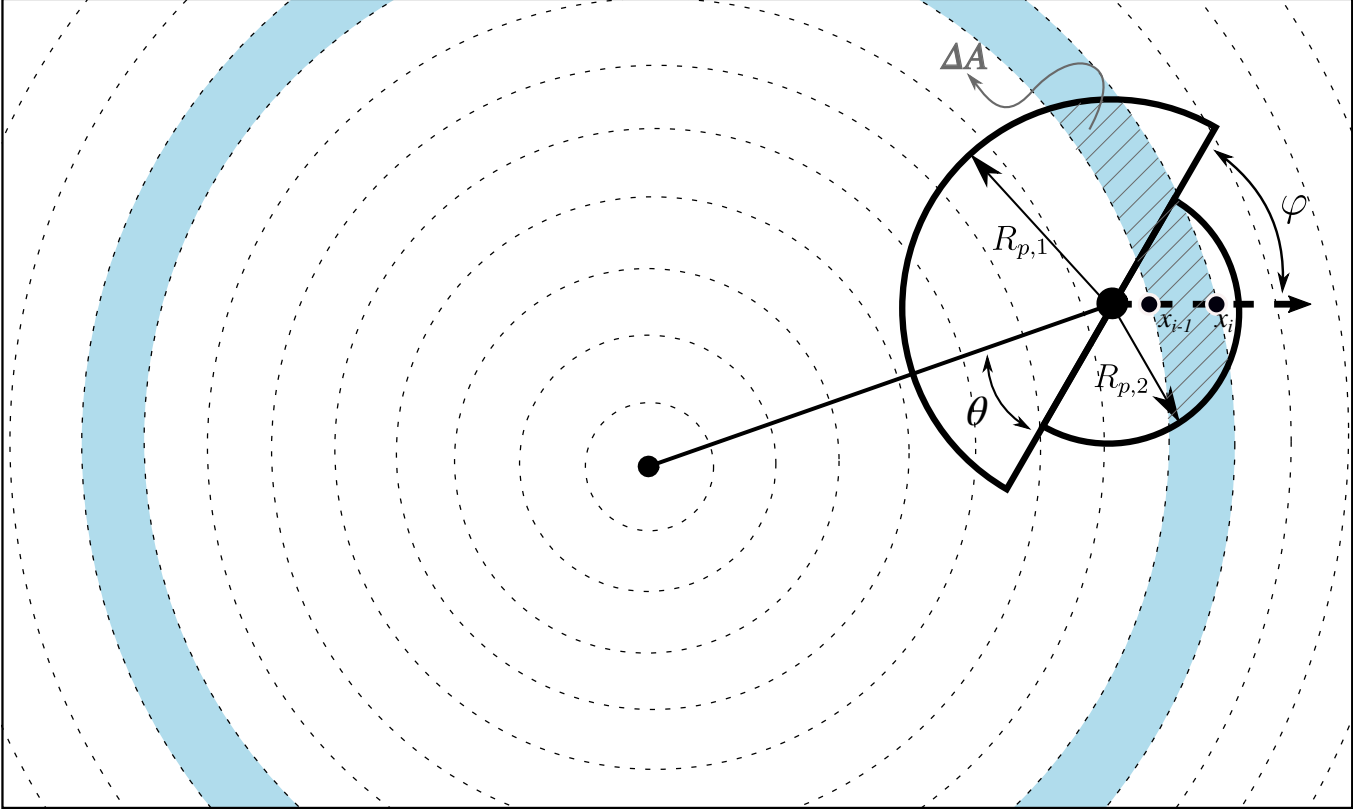


Figure 1. Diagram of the geometric configuration during transit of two stacked semi-circles (one of radius $R_{p,1}$; indicated by the arrow going up, and another of radius $R_{p,2}$; indicated by the arrow going down) that model the (possible) different limbs of an exoplanet transiting in front of a star. The area of the star has been divided in different sections of radius x_i (dashed circles) — between each subsequent section, the star is assumed to have a radially symmetric intensity profile (e.g., blue band between x_{i-1} and x_i above). In order to obtain the lightcurve such an object would produce, the challenge is to calculate the intersectional area between a given iso-intensity band and the stacked semi-circles, ΔA (blue band with dashed grey lines). Note the stacked semi-circles are inclined by an angle φ with respect to the planetary orbital motion (illustrated by the dashed arrow moving to the right), which accounts for the possibility of having planetary spin-orbit misalignments.

of dimensions (n_p, n_p) , on which we first fill all pixels within a distance of $n_p/2$ from the center of this matrix (i.e., $(n_p/2, n_p/2)$) with intensities given by the defined intensity profile (a quadratic law in the case of our implementation) — all other pixels are filled with zeroes. With this, we sum all the pixel values to compute our out-of-transit flux. Our algorithm then, using as inputs the coordinates of the center of the planet with respect to a reference frame centered on the star (X, Y) at each time-step and the input angle φ , computes the slope of the orbital motion $s = dY/dX$ by simple differences at each time-step i , i.e., $s_i = (Y_{i+1} - Y_i)/(X_{i+1} - X_i)$. This is then used to compute the instantaneous rotation of the axis that joins the stacked semi-circles with respect to the orthogonal system that defines the (X, Y) positions as $\arctan(s_i) + \varphi$. This axis is then used to separate the areas covered by both semi-circles, pixels inside of which are set to zero.

We use this simple numerical scheme to validate the semi-analytical framework developed in this work by

computing a set of cases including a challenging one in which the planetary orbit is significantly curved. This latter case allows us, in turn, to verify that our method outlined in Appendix A is correctly accounting for the rotation of the axis that joins the semi-circles with respect to the orthogonal system that defines the (X, Y) positions of the planet. To generate this, we simulate an exoplanet with a period of 3 days, time-of-transit center $t_0 = 0$, scaled semi-major axis $a/R_* = 1.5$ and zero eccentricity for three inclinations: $i = 55, 72$ and 89 degrees. For the star, we define a quadratic limb-darkening profile with $u_1 = 0.3$ and $u_2 = 0.2$. As for the physical properties of the planet, we assume it to have asymmetric terminator regions with $R_{p,1} = 0.1$, $R_{p,2} = 0.09$ and $\varphi = -45^\circ$. Planetary positions (X, Y) were obtained using `catwoman` (which uses the exact same method as `batman` to calculate them) for 100 equally spaced time-steps between -0.5 and 0.5 days. We performed numerical simulations with $n_p = 2500, 5000, 10000, 20000$ and 40000 (i.e., doubling the number of pixels on each side of

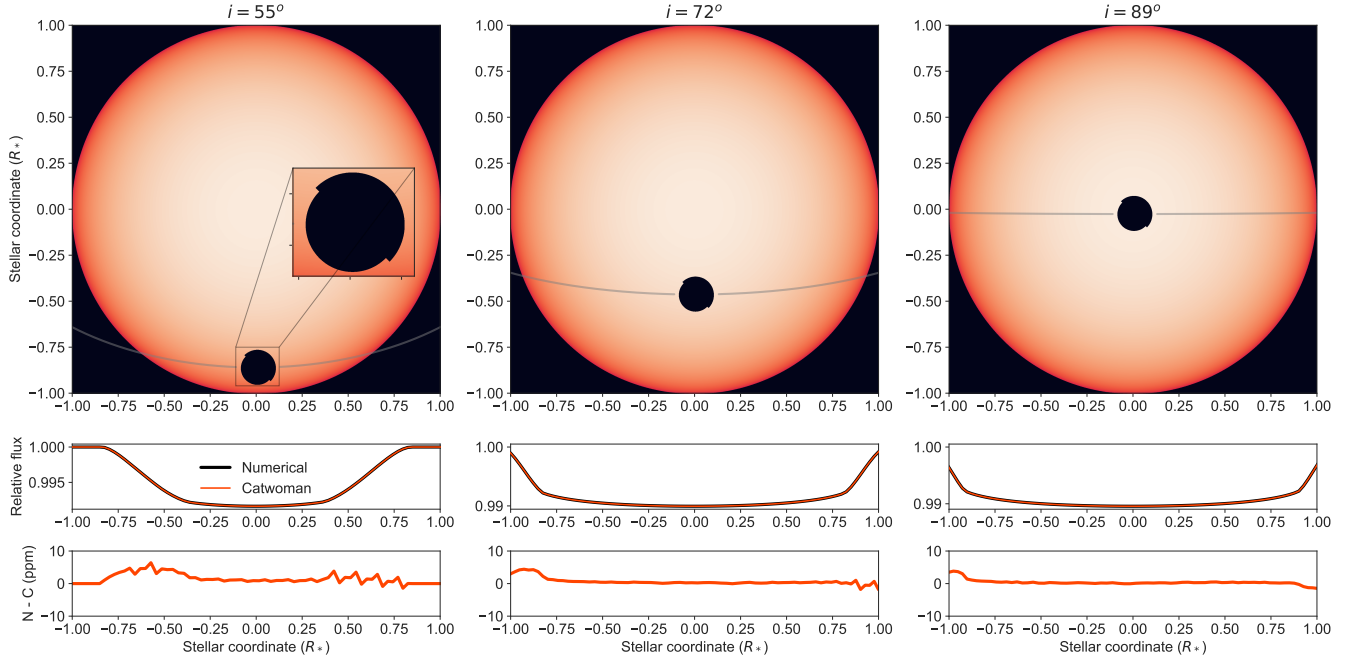


Figure 2. Comparison between a numerical implementation of the lightcurve generation of asymmetrical transits and the semi-analytical formalism presented in our work, implemented in the `catwoman` library. Examples are shown for orbital inclinations of 55° (left), 72° (middle) and 89° (right) — all of them assume a period of 3 days, a quadratic limb-darkening law ($u_1 = 0.3$, $u_2 = 0.2$), $a/R_* = 1.5$ and zero eccentricity. The top images are snapshots of our numerical model which include a limb-darkened star (orange) and a planet with asymmetric terminator regions ($R_{p,1} = 0.1$, $R_{p,2} = 0.09$ and $\varphi = -45^\circ$) transiting in front of it; middle panels show the retrieved lightcurves from both methods, and the bottom panels show the difference between the two. Most of the residuals observed in this latter panel are due to errors on our numerical model scheme (see text); by construction, our `catwoman` models in these computations had a 1 ppm error limit.

our matrix), and found that the maximum flux changes roughly halved as well between each of those runs. These changes reached 4 ppm between $n_p = 20,000$ and $n_p = 40,000$, which we consider as our maximum error on the fluxes of our numerical scheme when selecting this latter number for n_p . Simulations using both our numerical (with $n_p = 40,000$) and semi-analytical (through the `catwoman` library, with a maximum error set to 1 ppm) schemes are presented in Figure 2. As can be observed, the differences between both are *very* small; they reach peak differences of less than 5 ppm — most of which are explained by the errors defined by our numerical scheme.

For all practical purposes, these limits give us confidence that our semi-analytical framework works as expected for precisions which are better than current and near-future instruments such as *JWST*, which is expected to reach about 20 ppm lightcurve precisions (Greene et al. 2016). We note that the speed increase of the `catwoman` library in comparison to the numerical implementation is huge: `catwoman` takes a couple hundreds of milliseconds to generate a lightcurve in a 2.9 GHz Intel Core i9 processor. The numerical implementation takes tens of seconds to generate the same model. In gen-

eral, in experiments made with this processor, `catwoman` takes about twice the time `batman` takes to generate a lightcurve. This is consistent with the fact that the `catwoman` code-base is inherited from the `batman` one, and goes to show that the analytical part of `catwoman` is as fast as `batman`'s — only that we perform it twice, one for each of the stacked semi-circles.

3. DETECTABILITY OF THE EFFECT

Although the pioneering study of von Paris et al. (2016) already tried to detect the effect of asymmetric transit lightcurves produced by non-uniform cloud cover on precise data of three exoplanets obtained by the *Kepler* mission and *HST*, a systematic study of the detectability of the effect has not been done either on real or simulated transit lightcurves. Such a study is very timely as the *TESS* satellite (Ricker et al. 2014) just started its extended mission re-observing some of the most promising targets to detect this effect and as *JWST* prepares for launch. These missions have a key advantage over *Kepler*: they allow us to target objects with large scale-heights, for which this effect should be more prominent in the data even if they are observed over shorter time-scales.

The question of the detectability of the effect in a given dataset is, however, a complex one. It is not only related to the precision of the lightcurves themselves in order to be able to detect the effect (which is evident will depend on the difference between the effective size of the terminator region on the leading and trailing limb of the exoplanet), but also to the correlation between the parameters that could impact on a transit lightcurve. It could be that the lightcurve indeed is asymmetric but a given transit parameter is able to correct for this if a symmetric model is used. Indeed, [von Paris et al. \(2016\)](#) identified that the evidence for asymmetric lightcurves is heavily impacted by the knowledge of the ephemerides: a small shift in the time-of-transit center on a symmetric transit model could lead to an equally good fit to one with an asymmetric model, even for intrinsically asymmetric lightcurves. As such, in order to *claim* the detection of this effect, one needs to perform proper model comparison. In this work, we choose to use bayesian model evidences to this end. In particular, we assume both the symmetric and asymmetric lightcurve models are equiprobable a-priori, which implies the difference between the log-evidence of an asymmetric lightcurve, $\ln Z_A$ to the one obtained from a symmetric one, $\ln Z_S$, $\Delta \ln Z = \ln Z_A - \ln Z_S$, is equal to

$$\Delta \ln Z = \ln \frac{Z_A}{Z_S} = \ln \frac{\mathcal{P}(A|\text{Data})}{\mathcal{P}(S|\text{Data})},$$

where $\mathcal{P}(A|\text{Data})$ is the probability of the asymmetric model given the data and $\mathcal{P}(S|\text{Data})$ is the probability of the symmetric model given the data.

In what follows, we simulate asymmetric lightcurves using the `catwoman` library with *JWST*-like and *TESS*-like cadences, in order to study how the detectability of the effect changes with our knowledge of different parameters of the model and the lightcurve precision using bayesian evidences as the metric for detectability. We decide not to generate simulations for *HST*, as the gaps between orbits of the observatory imply a special, case-by-case analysis on the detectability of the effect — we leave such a study for future work. For each of the cases described below we generate asymmetric lightcurves with a range of radius differences between the leading (“morning”) and trailing (“evening”) limbs. We parametrize this in our simulations in terms of the corresponding “transit depth” each side of the planet implies. To this end, we fix $R_{p,1}/R_*$ to 0.1 in order to emulate a typical hot Jupiter planet-to-star radius ratio, and then define

$$R_{p,2}/R_* = \sqrt{(R_{p,1}/R_*)^2 + \Delta\delta}, \quad (2)$$

where $\Delta\delta$ is the morning-to-evening transit depth difference that in our simulations ranges from 10 to 1000

ppm in 30 log-spaced bins. For each of those combinations, we simulate 5 datasets of noisy transit lightcurves with noise levels σ_w ranging from 10 to 1000 ppm in 30 log-spaced bins as well. We calculate the average of the log-evidences for symmetric and asymmetric models fitted to that data in each $(\Delta\delta, \sigma_w)$ pair, which is then used to compute the difference between the log-evidences. In all of our simulations the period is set to 1 day, the semi-major axis to stellar radius ratio to $a/R_* = 10$, inclination to 90 degrees, and a circular orbit is assumed. We note this set of parameters define a worst-case scenario for the detection of the effect. The reason is that most of the information used to infer the limb asymmetries comes from ingress and egress, as has already been shown by previous works (see, e.g., [von Paris et al. 2016](#); [Kempton et al. 2017](#); [Powell et al. 2019](#)). The ingress/egress duration in a circular orbit is given by

$$\tau = \left(\frac{P}{\pi}\right) \left(\frac{1}{\sqrt{1-b^2}}\right) \left(\frac{R_p}{R_*}\right) \left(\frac{R_*}{a}\right).$$

In the case of these simulations, this gives an ingress/egress duration of only $\tau = 4.6$ minutes. As a comparison, the archetypal hot Jupiter HD 209458b ([Charbonneau et al. 2000](#); [Henry et al. 2000](#)) has $\tau = 25.7$ minutes. Our simulations in this Section, thus, can be seen as *lower limits* on the detectability of the effect. We explore the variation of the precision on the limb asymmetries with ingress/egress duration along with a case-study of a real hot Jupiter in Section 4.

To perform the fits to our simulated data, we implemented `catwoman` ([Jones & Espinoza 2020](#)) in the `juliet` ([Espinoza et al. 2019](#)) package, which already implements `batman` ([Kreidberg 2015](#)) for symmetric lightcurve models, and allows to compute bayesian evidences for our model comparison using MultiNest ([Feroz et al. 2009](#)) via the PyMultiNest wrapper ([Buchner et al. 2014](#)). We fix $\varphi = 90$ degrees for all simulations except the ones in Section 3.3. Uniform priors were defined for the planet-to-star radius ratios from 0 to 1.

3.1. Detecting asymmetric lightcurves with JWST

In order to perform the simulations for *JWST*-like observations, we needed to calculate a typical cadence for observations to be taken by the observatory for time-series exposures. In this work, we focus on observations aiming to constrain the effect using NIRISS/SOSS, as this unique instrument allows to obtain spectra all the way down to $0.6 \mu\text{m}$ through the combination of data from Order 1 ($1 - 3 \mu\text{m}$) and 2 ($0.6 - 1 \mu\text{m}$). Given the largest limb asymmetries seem to be in the transition between optical and NIR wavelengths (see, e.g., [Kempton et al. 2017](#); [Powell et al. 2019](#)), we believe this will

usually be the instrument of choice to characterize the effect for bright targets (with the alternative being, of course, NIRSpec/PRISM for fainter targets). Considering the reset time for this instrument is relatively short (couple of seconds), it sufficed for our work to know the typical integration time of a *JWST* observation with SOSS. For a solar-type, $V = 11$ star, according to the *JWST* Exposure Time Calculator⁵ (ETC; Pontoppidan et al. 2016), “saturation” is attained at about 20-60 groups per integration for NIRISS/SOSS, which implies maximum integration times between 40-80 seconds per datapoint in the time-series. We arbitrarily decided to use 20 seconds for the cadence of our simulations in order to simulate observations trying to target half-saturation values, which has been a typical strategy for *HST* observations⁶.

In this case we tried three different simulations, in order to illustrate the impact of different assumptions in this one-transit, 20-second cadence case: (a) one in which everything but the radii of both sides of the exoplanet $R_{p,1}$ and $R_{p,2}$ are known, (b) one in which everything but the radii and the limb-darkening coefficients of the star are known, and finally (c) one in which everything but the radii, the limb-darkening coefficients of the star and the time-of-transit center are known. The limb-darkening law that was assumed to generate and fit the lightcurves was a quadratic law with $(u_1, u_2) = (0.3, 0.2)$, which are representative values for solar-type stars. In our *juliet* fits, we assumed the uninformative priors for two-parameter limb-darkening laws proposed by (Kipping 2013) for the cases in which limb-darkening was assumed to be unknown; for the time-of-transit center, a uniform prior with a width of 5 hours around the real predicted time of transit center was imposed. The results for these simulations are presented in Figure 3.

As can be observed from the simulations, the asymmetric transit lightcurves should be detectable (i.e., $\Delta \ln Z \gtrsim 2$) for morning-to-evening depth differences above around 50 ppm for a wide range of precisions at least in white-light (i.e., adding all the flux over the entire wavelength range of a given instrument), where *JWST* observations should achieve tens of ppm precisions per point in the transit lightcurves, and as long as the ephemerides are well known and constrained. If they are not, however, as can be observed in the rightmost panel of Figure 3, the actual detection of the effect

becomes extremely challenging because, as it has been already noted by von Paris et al. (2016), changes in the time-of-transit center in a symmetric model can account for the asymmetry in the lightcurve. The changes in this timing are very small — only a couple of seconds of shifts in the time-of-transit center suffice to mimic the asymmetry in the transit lightcurves (see Section 4.3 for details). This implies that to detect this effect in white-light, very precise timings are needed in order to claim a detection.

It is important to note that although from the above results the detection of the effect *directly* in the white-light lightcurves even with *JWST*-like precisions seems challenging to do with only one transit in the absence of precise timing constraints, the observatory has the advantage that it can perform spectro-photometry and, thus, the effect can be detected through the wavelength dependence of the radii at each side of the terminator region, as has already been highlighted by Powell et al. (2019) — see also Section 4. In particular, NIRISS/SOSS can produce extremely precise (tens of ppm) white-light transit lightcurves in Orders 1 and 2, which can be used to claim a detection of the effect using these white-light transit lightcurves alone.

3.2. Detecting asymmetric lightcurves with *TESS*

Although the *TESS* mission has a significantly smaller aperture than *JWST*, the cadence and types of observations the mission does are excellent for the detection of asymmetries in transit lightcurves. The mission not only attains an exquisite precision, but it is also able to observe several transits of the same exoplanet, leveraging the problem we observed with only one transit in *JWST*-like observations like the ones simulated in the previous subsection. We performed the same simulations that we did for *JWST* but with a *TESS*-like cadence of 2-minutes, where we only consider observations on a 27-day period (i.e., one *TESS* sector). Interestingly, the three cases that we tried in the previous sub-section (all known, all but limb-darkening known and all but limb-darkening and the time-of-transit center known) all resulted in practically identical results — we show the one corresponding to the case in which all the parameters are assumed to be known but the radius, the limb-darkening coefficients and the time-of-transit center in Figure 4.

As can be observed, the results are very similar to the ones of *JWST*. This is a combination of the fact that there is about a 27-fold increase in the number of transits, which helps with the 6-fold increase on the cadence of the observations as compared to the *JWST* ones. The fact that there are more transits, in addition, helps with

⁵ <https://jwst.etc.stsci.edu/>

⁶ But see <https://jwst-docs.stsci.edu/methods-and-roadmaps/jwst-time-series-observations/tso-saturation>.

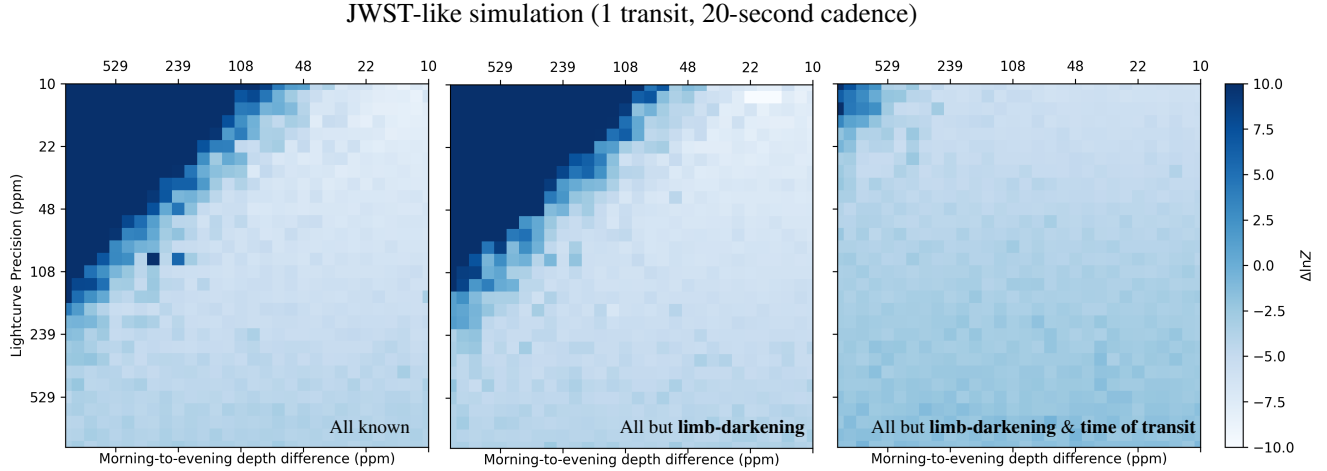


Figure 3. Simulations of asymmetric lightcurves due to differences in the morning and evening terminator transmission spectra for *JWST*-like cadence (1 transit, 20-second cadence, 1-day period, 4.6-minute ingress/egress duration) when all the parameters other than the planetary radius is known (left), other than the planetary radius and limb-darkening (center) and other than the planetary radius, limb-darkening and time-of-transit center (right). Colors indicate the difference between the log evidences of asymmetric models and symmetric models (positive meaning odds ratios in favor of asymmetric lightcurve models). Note how if the time-of-transit center is unknown all the possible evidence for detecting the effect vanishes unless the lightcurve precision is extremely high, which will most likely make it impossible to detect this effect in white-light alone with *JWST* unless simultaneous observations are taken or strong timing priors are known.

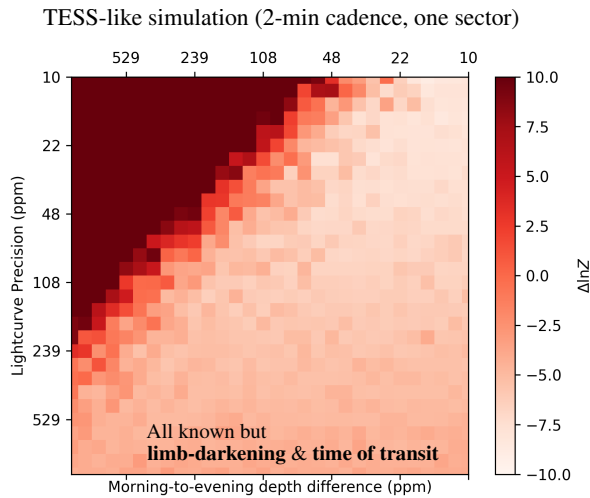


Figure 4. Simulations of asymmetric lightcurves due to differences in the morning and evening terminator transmission spectra for *TESS*-like cadence (2-minute cadence, one sector, 1-day period, 4.6-minute ingress/egress duration) when all the parameters other than the planetary radius, limb-darkening and time-of-transit center are known. Colors indicate the difference between the log evidences of asymmetric models and symmetric models (positive meaning odds ratios in favor of asymmetric lightcurve models).

the problem *JWST* will face related to the ephemerides where in our analysis, of course, there is an implicit assumption regarding no possible deviations from strict periodicity in the transit times.

Although few targets attain the precisions at which one might statistically distinguish between an asymmetric and a symmetric model directly from the transit lightcurves with *TESS* in one sector, the fact that many targets are observed by more than one sector makes this effect within reach of what *TESS* is currently able to detect. Targets in the *JWST* Continuous Viewing Zone (CVZ) are particularly appealing to try to detect this effect.

3.3. Detectability assuming φ is not known

As a final test on the detectability of the effect, we explore whether our ignorance on the angle φ can impact on the level of detectability of the effect; we take our *JWST*-like simulation as a proxy for studying this, given the similarity in the shape of the detectability maps presented between *JWST* and *TESS* in Figures 3 and 4. To explore this, we use a transit lightcurve whose parameters are defined by the same ones as in the previous experiments, but in this case we set $\varphi = 45$ as the ground-truth, and set a uniform prior between -90 and 90 degrees for the parameter in our fits. Our results for a *JWST*-like simulation (using the same cadence as in Section 3.1) are shown in Figure 5.

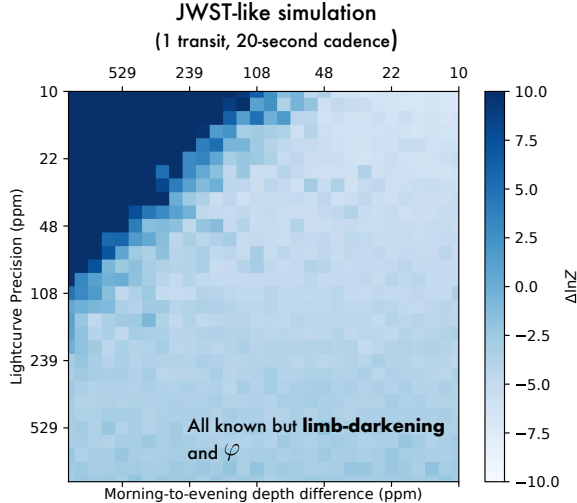


Figure 5. Simulations of asymmetric lightcurves due to differences in the morning and evening terminator transmission spectra for a *JWST*-like cadence (20-second cadence, one transit, 1-day period, 1-hour transit duration) when all the parameters other than the planetary radius, limb-darkening and angle φ known. Colors indicate the difference between the log evidences of asymmetric models and symmetric models (positive meaning odds ratios in favor of asymmetric lightcurve models).

As can be seen, the detectability region (i.e., the medium blue and dark-blue region) of the plot has shifted by a small amount with respect to the one presented in Figure 3 implying that a slightly better lightcurve precision is needed in order to detect the effect if the angle φ is not known a-priori. In practice, for the experiments made in this section, this implies that with a 20 ppm lightcurve precision one would be able to detect depth differences on the order of 200 ppm instead of the 100 ppm differences implied when the angle is known. As will be shown in Section 4.1, the odds of detecting the effect on systems which have better prospects for it (i.e., systems with longer ingress/egress durations) are in reality much higher. The lower limits we set here, thus, seem promising for the detection of the effect with current and near-future instrumentation.

4. DISCUSSION

In previous sections, we have presented both the details of our semi-analytic framework for generating asymmetric transit lightcurves due to morning/evening terminator heterogeneities — including its validation against simpler (but more computationally expensive) models — and a study of the detectability of the effect with current missions like *TESS* and future observatories like *JWST*. Although our results are encouraging for the detection of the effect, there are many aspects to pay attention to when performing lightcurve analyses

and/or when planning observations to detect the effect, including complementary methodologies, which we discuss below.

4.1. Asymmetric terminator depths precision

While in Section 3 we presented lower limits on the statistical detection of the effect on transit lightcurves based on bayesian evidences, an important aspect of interpreting transit lightcurve fits with the semi-analytic model presented in this work will involve constraining the actual measured transit depths of each side of the planet. This will be useful not only to extract transit spectra of the different limbs when using wavelength-dependent lightcurves such as the ones to be obtained by *JWST*, but also to compute the maximum possible transit depth differences allowed by the data when analyzing broadband data such as the one from missions like *TESS*.

An important detail to consider when extracting transit depths from asymmetric limbs is the fact that the observable quantities that are directly constrained by the data are the areas of each of the semi-circles through the transit depths each of them produce. In symmetric models, where the limbs are assumed to be equal, the transit depth is simply $\delta = (R_p^2/R_*^2)$ — the projected area of the planet over the projected area of the star. In the asymmetric case, however, the projected area of the *semi-circles* are the quantities of interest, — the transit depth of each limb being given by $\delta_i = (1/2)(R_{p,i}^2/R_*^2)$. This is what effectively defines the transit spectrum of each limb and is, in turn, what should be used to compare against theoretical transmission spectroscopy models.

Figure 6 shows how the precision of the transit depths of each limb depend on the lightcurve precision, as well as the precision of the entire area of the planet, defined by the depth $\delta_1 + \delta_2$, for the case of the exoplanet simulated in Section 3 with an ingress/egress duration of $\tau = 4.6$ minutes (solid lines). As can be seen, the precision on the transit depth of the entire planet is always much smaller than the corresponding for both semi-circles, but the relationship between the two is not simple, as the transit depths of the semi-circles are highly correlated with each other. Indeed, the transit depth of the entire planet is constrained by *the entire lightcurve*, whereas the transit depths of each side of the planet (sampled by the semi-circles in our model) are mostly constrained by ingress and egress. This implies, in turn, that this latter precision would of course increase on systems with larger ingress/egress durations, which in many cases might be the optimal ones to target in order to maximize the chances to unveil this effect.

The simulations presented in Section 3 for $\tau = 4.6$ min. ingress/egress durations were performed to show lower-limits on the detection of the effect, and even in those cases the odds were very favorable given current (e.g., *TESS*) and future (e.g. *JWST*) lightcurve precisions and cadences. Hot Jupiters typically have longer ingress/egress durations, and some of the already characterized ones by missions like, e.g., *HST*, show good prospects for the detection of the effect as well. As an example, we repeat the *JWST* simulations in Section 3 for HAT-P-41b, which has recently been characterized both at optical and near-infrared wavelengths by Wakeford et al. (2020) and Sheppard et al. (2020), respectively. We tune the physical and orbital parameters of the system to the ones used in Wakeford et al. (2020), which imply a 23.9 min. ingress/egress duration. The cadence (53 seconds) and number of datapoints (500) for our simulations are set to the ones optimized by PandExo⁷ (Batalha et al. 2017) using NIRISS/SOSS as the instrument of choice such that SUBSTRIP256 does not saturate (which would be the setup of choice in order to obtain simultaneous spectroscopy in the near-infrared and the optical through Orders 1 and 2 for this target⁸). For consistency, we set the limb-darkening coefficients to the average ones on Order 1 of NIRISS/SOSS (but we note these do not impact on the overall precision and detectability, as was already shown in Section 3). The resulting precisions of this experiment are presented in Figure 6 as dashed lines. As can be observed, the precision change on the transit depths of each of the limbs is significant, and ranges from a 60% to 70% improvement in it. The precision change in the transit depth of the entire planet, however, is much smaller (and driven mainly by the difference in the absolute transit depths and transit durations), which acts as a baseline in showing quantitatively how the prospects of detecting asymmetric limb-differences are very sensitive to the ingress/egress duration.

One might argue that in Figure 6, one could observe two transits of the exoplanet with 4.6 min. ingress/egress duration in order to match the signal-to-noise of the exoplanet with the 23.9 min. ingress/egress duration. Although this would be true if the observatory only targeted the transit event, in practice there are observational overheads (like, e.g., pre-post transit baselines, and overall observatory overheads beyond clock time on-target) that have to be included in that reason-

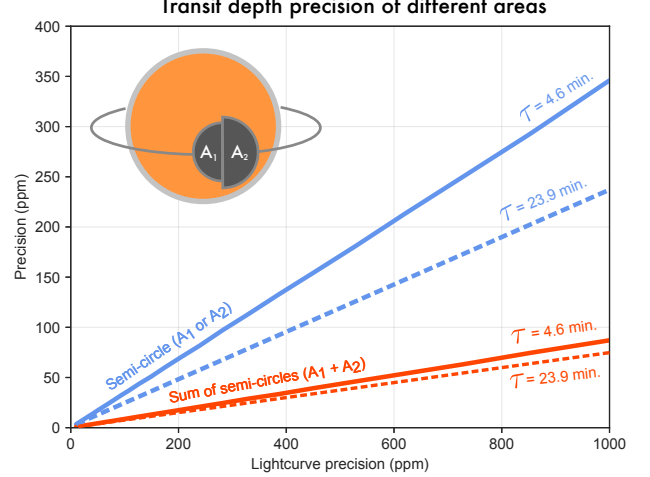


Figure 6. Transit depth precision on the semi-circles (transit depth defined as $\delta_i = (1/2)(R_{p,i}/R_*)^2$, with $R_{p,i}$ being the area of semi-circle i ; blue lines) and their sum (whose transit depth is $\delta_1 + \delta_2$; red lines) as a function of lightcurve precision. Precisions for systems with short (4.6 min., solid lines) and long (23.9 min., typical for hot Jupiters) transit ingress/egress durations, τ , are presented. **Main point:** Transit depth precisions of the limb of exoplanets are much less precise and much more dependant on transit ingress/egress duration than the transit depth produced by the entire area of the planet (i.e., the classically defined “transit depth”).

ing. For instance, the time recommended in the *JWST* documentation⁹ one should spend in a target during a transit is given by the dwell equation, which reads

$$T_{\text{dwell}} = 0.75 + \text{MAX}(2, T_{14}) + T_{14} + 1 \text{ hr}, \quad (3)$$

where T_{14} is the transit duration in hours. The exoplanet with an 4.6 min. ingress/egress duration has a 1-hour total transit duration, which gives $T_{\text{dwell}} = 4.75$. The exoplanet with a 23.9 min ingress/egress duration has a 3.6-hour transit duration, $T_{\text{dwell}} = 8.95$. Two transits of the 1-hour transit duration target would imply a requested time of 9.5 hours, which is at least half an hour more expensive than the 3.6-hour transit duration target — all this without considering extra observatory overheads. The conclusion, thus, is that the efficiency of the time and targets to be requested to detect the effect have to be studied on a case-by-case basis.

4.2. The importance of constraining limb transit spectra

In order to showcase the importance of directly using transit lightcurves to constrain the limb of exoplanets,

⁷ <https://exoctk.stsci.edu/pandexo/>

⁸ We note HAT-P-41b saturates below about 2 microns with NIR-Spec/PRISM, which is the reason why we don’t discuss this instrument in the context of this exoplanet.

⁹ <https://jwst-docs.stsci.edu/>

and demonstrate that this indeed might be *the most efficient avenue to constrain the transit spectrum of the limbs*, we use HAT-P-41b as a case-study, using the simulations described in the previous sub-section. We use the PandExo outputs in order to estimate the lightcurve precisions on each wavelength bin for Order 1, and extract the corresponding signal-to-noise ratios (and thus lightcurve precisions) for Order 2 using the *JWST* Exposure Time Calculator (ETC¹⁰). We then use the relationship found in Figure 6 in order to predict the expected precision on the “limb spectrum” at each wavelength bin. Motivated by the works of Kempton et al. (2017) and MacDonald et al. (2020), we search for the best-fit model to the *HST* data of HAT-P-41b presented in Sheppard et al. (2020) using *two* different atmospheric structures, each of which represents one of the limbs. We choose to use the ATMO models¹¹ described in Goyal et al. (2018) to represent each of them, whose transit depths are scaled to 1/2 in order to compute the spectra of each of the limbs, δ_i . We allow for all the parameters of the models to vary between the limbs except for the metallicity, which we assume should be the same across the planet (and thus, across the limbs) in this experiment. We perform model fits to the data presented in Sheppard et al. (2020) using the combined spectrum of the limbs, $(\delta_1 + \delta_2)$, via simple (weighted) least-squares minimization, and select the set of “best-fit” models via the Bayesian Information Criterion (BIC, Schwarz 1978) — all models with a BIC within 2 of the model with the minimum BIC are defined in our set of “best-fit” models (~ 200 different models). A pair of representative models from this subset are presented on the left top and bottom panels of Figure 7 which, as can be seen, provide a reasonably good fit to the data, and are very similar to the best-fit retrieval models presented both in Sheppard et al. (2020) and Wakeford et al. (2020). The corresponding limb spectra that produced those combined spectra, along with a simulated limb spectrum with *JWST* NIRISS/SOSS precisions (in only 2 transits), are presented in the top and bottom right panels of Figure 7.

Before explaining the details of the models that generated the presented fits to the data, it is important to note how the best-fit models on the left panel of Figure 7 (i.e., Model 1 and Model 2) are almost indistinguishable, with differences between the models being generally at

the $\lesssim 30$ ppm level on the transit depths at the wavelengths presented in these figures. These differences, in turn, are at the limit of what NIRISS/SOSS can do in only two transits on the presented wavelength ranges and at the resolutions needed to distinguish these models. Using our PandExo and ETC calculations, we estimate that over three to four transits would be needed to reliably differentiate between them if only the transit depths (i.e., left panels) were used to infer the presence of these two limbs. However, as can be seen in the right panels of Figure 7, the limb models give rise to markedly different spectra in this wavelength range. The top ones originate from a situation akin to that envisioned by Kempton et al. (2017), in which a hotter evening side is covered in photochemical hazes transported from the dayside, whereas the morning side is either free of those or could have some degree of cloudiness depending on the temperature in the morning limb. The limb models on the bottom show the non-hazy but cloudy cases, illustrating also the impact of the limb temperatures; whereas the top limb models show very similar temperatures (and thus, overall similar features in the limb spectra), the bottom limb models show markedly different features, especially in the optical part, where TiO condensation in the colder (presumably the morning) limb precludes it from showing large features in the spectrum, marking a sharp difference that should be observable in Order 2 of NIRISS/SOSS in this case.

Of course, one approach to test the plausibility of those two (and the rest of the “best-fit”) models could be to study Global Circulation Models (GCM). While we believe there is additional value in such a comparison that could help guide possible observations of this effect, a study in that direction is outside the scope of this work. We would like to note, however, that GCM modelling assumptions and implementation details have been actively driven by observations in the past few years. For instance, until recently clouds and hazes were typically added in a post-processing stage, not including feedback from these components in the modelling. Recent works such as those of Roman & Rauscher (2019) and Parmentier et al. (2020) have managed to implement clouds in their GCMs directly, showing in turn that this is critical to understand the overall cloud structure itself and heat redistribution in the planets under study, which has provided a much better match to observed phase-curve observations. We believe this highlights the importance of extracting limb spectra for the overall modelling of exoplanetary atmospheres: it could provide complementary data to that already provided by phase-curves, that 3D models of exoplanetary atmospheres could aim to reproduce. In the case of our ex-

¹⁰ <https://jwst.etc.stsci.edu/>

¹¹ In particular, we use the set of models tailored to HAT-P-41b using rainout condensation, where condensed species deplete the gaseous elemental abundances that give rise to features in the spectrum.

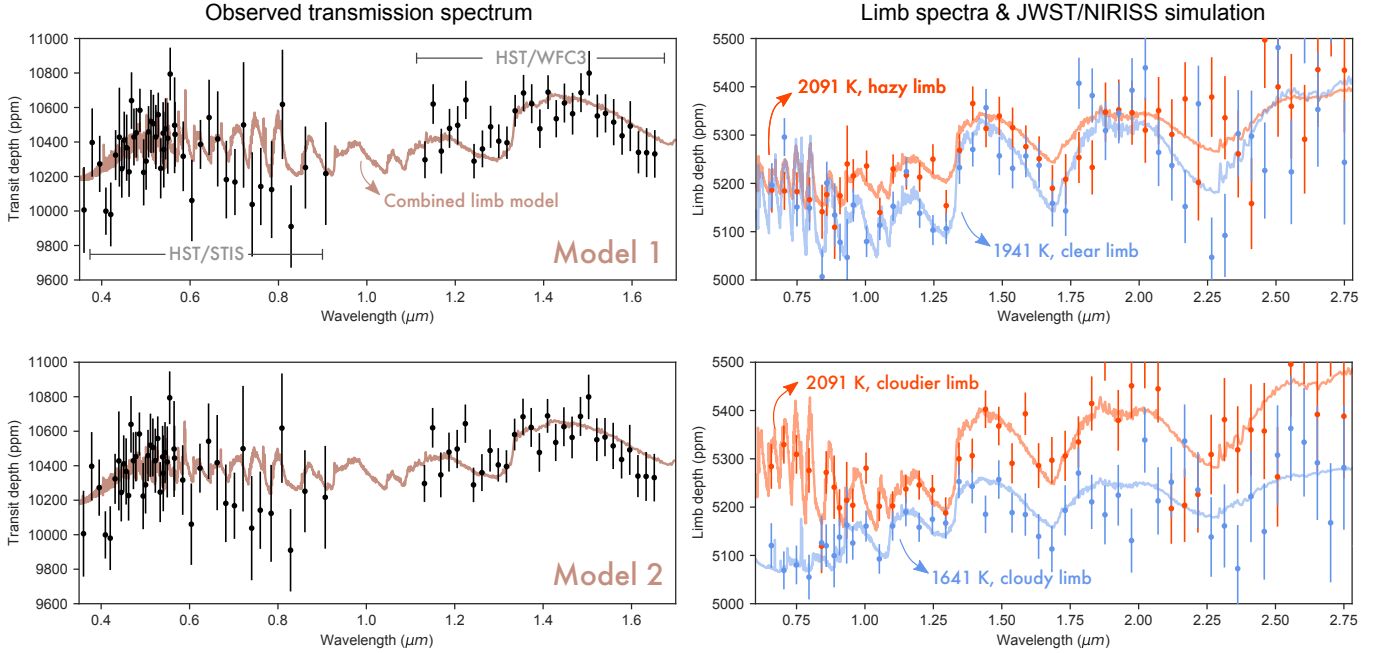


Figure 7. (Left) Observed transit spectrum by *HST* STIS ($< 1.0 \mu\text{m}$) and *HST* WFC3/IR ($> 1.0 \mu\text{m}$; black points with errorbars) of HAT-P-41b presented in Sheppard et al. (2020), along with two models (brown — Model 1; top, Model 2; bottom) that give rise to reasonably good fits to the data. These models, δ , are a combination of two different sets of limb spectra, presented in the right panels (top for the set of limb spectra generating Model 1, bottom for the set of limb spectra generating Model 2). They are practically indistinguishable at the wavelengths presented in these panels at the $\lesssim 30$ ppm level (see text). (Right) Limb spectra generating the models in the left panels. Colored datapoints present simulated limb spectra extracted directly from the lightcurves using NIRISS/SOSS. **Main point:** two very different sets of limb spectra (top right and bottom right panels) can give rise to practically indistinguishable transit spectroscopy models (top left and bottom left panels, respectively). Extracting the limb spectra with the methods presented in this work is possible (points with errorbars in the right panels), and is in this case perhaps the most efficient way to characterize the terminator region(s) of this exoplanetary atmosphere.

ample in Figure 7, for instance, observations like these, where independent temperatures could be extracted for the morning and evening limbs, could help understand the overall heat transport efficiency in exoplanet atmospheres in the presence of clouds, which could provide additional evidence to test theories of how this evolves with equilibrium temperature (see, e.g., Parmentier et al. 2020, and references therein).

We note that observations aiming to extract these limb spectra can be much cheaper than, e.g., phase-curves. Whereas two NIRISS/SOSS transits for HAT-P-41b, for instance, would amount to a total science time to a *JWST* proposal of about 17.5 hours (using Equation 3), a full phase-curve for this particular exoplanet requires over 65 hours. In this sense, extraction of limb spectra could serve as a good diagnostic as to what to expect in a phase-curve observation *before* performing these expensive observations. Since for a fixed planetary and stellar radii the ingress/egress duration increases with the square-root of the semi-major axis (i.e., $\tau \propto \sqrt{a}$), this technique for detecting limb

asymmetries might in turn be an excellent alternative avenue to studying morning and evenings of longer period planets where phase-curve signals are too small to be detectable in a reasonable amount of time.

4.3. Timing variation biases due to asymmetric terminator depths

In Section 3 we discussed how, as predicted by von Paris et al. (2016), small changes in the time-of-transit center can give rise to equally good fits on symmetric models (such as the ones assumed by the *batman* package, for instance), even if the data is truly arising from an asymmetric transit model. It is important to note that this in turn can give rise to biases in transit times if a symmetric model is used when the data in fact comes from an asymmetric model such as the one modelled by the *catwoman* library. In our simulations, these can give rise to timing offsets of up to 5 seconds, which is in turn within the timing precision that the *TESS* mission is able to reach, and will be for sure within reach of the *JWST* mission. Care must be taken, thus, when search-

ing for small (second-level) timing offsets in these precise transit lightcurves in the search of, e.g., transit timing variations.

4.4. *Limitations of this study*

It is important to note that throughout this work, we have assumed that the only alternative model to that of limb asymmetries is that of a symmetric limb in order to explain transit lightcurves asymmetries. However, there are other competing effects that might give rise to asymmetric lightcurves as well. For instance, known stellar effects such as gravity darkening (see, e.g., Ahlers et al. 2020, and references therein) and yet-to-be uncovered effects/properties such as exoplanetary rings (see, e.g., Rein & Ofir 2019, and references therein) can also give rise to asymmetric lightcurves. Performing a detailed model comparison study between these effects and the one studied here is out the scope of this work, but we warn researchers that proper care must be taken when aiming to claim the detection of asymmetric limbs in light of these possibilities. While effects like, e.g., gravity darkening are most likely known at good enough precisions in order to understand when a given transit lightcurve might be asymmetric due to this effect or at the very least to put limits on asymmetries generated by it, known unknowns such as exoplanetary rings might be more complicated to rule out. Perhaps the easiest way to constrain this would be through the wavelength-dependance of these asymmetries, which we hypothesise should be markedly different in the case of exoplanetary rings and those produced by opacity sources in an exoplanetary atmosphere. Still, it is important to be mindful of these alternative hypotheses when analyzing data on the search of these lightcurve asymmetries.

5. CONCLUSIONS

In this work, we have presented a detailed study on the observational prospects of directly detecting transit lightcurve asymmetries due to inhomogeneous exoplanetary limbs with current and near-future instrumentation. A semi-analytical framework was introduced in Section 2 to fit transit lightcurves in order to extract the transit depths of the different limbs, a problem which is approximated as a pair of stacked semi-circles of different radii transiting a limb-darkened star following von Paris et al. (2016). Implemented in the *catwoman* python library (Jones & Espinoza 2020), this framework allows for the fast computation of these lightcurves, which are even able to model the rotation of the axis that joins the semi-circles, being thus able to characterize sky-projected planetary spin-orbit misalignments in a complementary fashion to that allowed by the eclipse

mapping technique for both lightcurves (Rauscher et al. 2007; Williams et al. 2006) and radial-velocities (Nikolov & Sainsbury-Martinez 2015).

A detailed feasibility study was presented in Section 3 for detecting the effect with current existing facilities such as *TESS* and near-future observatories such as *JWST*. Even in a worst-case scenario of a planetary transit with a very small ingress/egress duration (which is the portion of the lightcurve that mainly constrains the limbs), the prospects for detecting the effect are very promising, even considering our ignorance on the angle that defines the sky-projected planetary spin-orbit misalignment. If aiming at detecting the effect with only one transit, however, care must be taken as the time of transit center is highly degenerate with the limb asymmetries (i.e., a small shift in the time-of-transit can give rise to a similarly good fit to that of an asymmetric lightcurve due to inhomogeneous limbs).

Finally, we showed in Section 4 how important the transit ingress/egress duration is for the detection of the effect. We used HAT-P-41b as a case-study to showcase the prospects for extracting the spectra of each of its limbs, and concluded that analyzing the lightcurves directly with the methods presented in this work might be one of the most efficient ways to obtain a global picture of each of the limbs, with *JWST*-like precisions enabling the extraction of their spectra given the exquisite spectrophotometric precision the observatory will be able to achieve.

We believe the promise of being able to characterize the limbs of exoplanets could play a pivotal role in our understanding of the 3-dimensional structure of exoplanets, and could provide observations that can inform current (e.g., GCM, transmission spectroscopy models) and future (e.g., phase-curves) models and observations aimed at the characterization of exoplanet atmospheres. The technique might, in turn, be a much less time-demanding technique to probe the 3D structure of longer period exoplanets, where phase-curves can be prohibitively expensive. Overall, we believe exploring the detectability of the effect in real transit lightcurves is critical to understand the limitations of the technique of transit spectroscopy when it comes to interpreting structural profiles such as temperature/pressure profiles and abundances in a 1-dimensional fashion (MacDonald et al. 2020). This, in turn, will be fundamental to make claims regarding formation mechanisms of these exoplanets based on the latter (Öberg et al. 2011; Espinoza et al. 2017; Mordasini et al. 2016), and their overall dependance with planetary properties (see, e.g., Sing et al. 2016; Welbanks et al. 2019, and references therein).

ACKNOWLEDGMENTS

We would like to thank L. Carone and P. Mollière for fruitful discussions on the theory of transmission spectroscopy and 3D modelling as applied to asymmetric limbs, as well as L. Kreidberg, T. Loudon, D. Powell and N. Nikolov on fruitful discussions regarding constraining limb inhomogeneities directly from transit lightcurves. N.E. would like to thank the IAU and the Gruber foundation for the support to this research through the IAU-Gruber Fellowship, with which this work was started. Finally, we would also like to thank the MPIA Summer Program for the support to start this research.

APPENDIX

A. DERIVING ΔA

In order to derive the decrement of flux due to the transit of a pair of stacked semi-circles given by equation 1, we must find ΔA , the inter-sectional area between the stacked semi-circles and the iso-intensity band depicted in Figure 1. As already noted by Kreidberg (2015) in the case of a circle, this area is simply the inter-sectional area of the stacked semi-circles with the circle of radius x_i , $A(x_i, R_{p,1}, R_{p,2}, d, \varphi)$, minus the same inter-sectional area but with the circle of radius x_{i-1} , $A(x_{i-1}, R_{p,1}, R_{p,2}, d, \varphi)$, i.e.,

$$\Delta A = A(x_i, R_{p,1}, R_{p,2}, d, \varphi) - A(x_{i-1}, R_{p,1}, R_{p,2}, d, \varphi).$$

This implies that to find ΔA one has to first find a general form for the inter-sectional area between the stacked semi-circles and a circle. These stacked semi-circles, in turn, are composed of two semi-circles, and thus the problem reduces to calculating the area of the intersection between a circle and two (rotated) *semi-circles* with a common center: one of radius $R_{p,1}$ and another of radius $R_{p,2}$, but rotated by 180 degrees. Given a general formula for such intersection, $A_S(R, R_S, d, \theta)$, where R is the radius of the circle, R_S the radius of the semi-circle, d the distance between the center of the circle and the semi-circle and θ the rotation angle of the semi-circle with respect to d , then

$$A(x, R_{p,1}, R_{p,2}, d, \varphi) = A_S(x, R_{p,1}, d, \varphi) + A_S(x, R_{p,2}, d, \varphi + \pi).$$

If we find a general form for $A_S(\cdot)$, then we solve the problem. We tackle this problem in the next sub-section.

A.1. Intersection area between a circle and a semi-circle

Although the case of calculating the intersection area between two circles can be obtained via elemental trigonometry, the problem of calculating the intersection area between a circle and a (rotated) *semi-circle* is not, in general, as straightforward.

We first note that the problem of finding the intersection area of a circle of radius R and a semi-circle of radius R_S rotated by an angle θ with respect to the line that joins the centers of length d is the same problem as the intersection area of a semi-circle and a *circle rotated by an angle θ with respect to the line that joins the centers*. This symmetry argument allows us to put the horizontal axis of this problem in the base of the semi-circle, simplifying the notation of the problem. Without loss of generality, we put the origin in the center of the base of the semi-circle. This transformed geometry of the problem is shown in Figure 8; here the white dashed area inside the semi-circle is the area of interest (i.e., the one that leads to $A_S(R, R_S, d, \theta)$).

As is evident in Figure 8, there are three different cases (a, b and c) we have to take care of in order to find a general formula for $A_S(R, R_S, d, \theta)$:

- Case (a), divided into sub-cases (a-1), (a-2) and (a-3), deals with the problem in which the circle is rotated such that it lies above the semi-circle. If we identify the coordinates of the center of the circle as $(x_0, y_0) =$

$(-d \cos \theta, d \sin \theta)$, case a) deals with the problem in which $\theta > 0$ and, thus, $d \sin \theta > 0$. Here, the intersection points between the circle and the semi-circle have coordinates (a_1, b_1) and (a_2, b_2) . The geometry depicted in Figure 8 for this case implies that $b_1 = 0$. This is because for $b_1 > 0$, the problem is the same as the intersection of two circles (one of radius R and another of radius R_S), which has a known analytical solution (see, e.g., Kreidberg 2015). Here the area of interest, A_S , is given by the area of the semi-circle ($\pi R_S^2/2$) minus $A_1 + A_2$ for case (a-1) and by $A_1 + A_2 + A_3$ for cases (a-2) and (a-3). The different sub-cases depend, in turn, on the location of the intersection points and the position of (a_3, b_3) , the position of the maximum extension of the circle in the x-axis.

- Case (b) deals with the problem in which the circle is rotated such that it lies *below* the semi-circle, i.e., where $\theta < 0$ and, thus, $d \sin \theta < 0$. In addition, this case handles only problems in which one intersection of the circle with the semi-circle is in its base and the other is with the upper part of the semi-circle. Once again, the intersection points between the circle and the semi-circle have coordinates (a_1, b_1) and (a_2, b_2) . In this case, however, $b_2 = 0$; the cases in which $b_2 \neq 0$ (i.e., when the right-most intersection is on the upper part of the semi-circle) and in which $b_2 = 0$ and $b_1 = 0$ (i.e., in which the left-most intersection is also on the base of the semi-circle) is taken care of by case c). The area of interest for case (b) is $A_S = A_1 + A_2$.
- Finally, case (c), divided into sub-cases (c-1), (c-2) and (c-3), deals with the problem in which the circle is either rotated above or below the semi-circle, but where there are two intersections with both either in the base (c-1) or in the upper part of the semi-circle (c-2) or four intersection points (c-3) between the circle and the semi-circle. In this case, the area of interest, A_S can be calculated directly via basic trigonometry and thus we don't identify here the intersection points by coordinates but by the red points in order to guide the reader.

Cases (a), (b) and (c) defined above will all be calculated assuming that the center of the circle is to the left of the semi-circle. The reason for doing this is that the problem has reflective symmetry with respect to the line that goes through the center of the semi-circle and that is perpendicular to its base. As such, for $0 < \theta < \pi/2$ we have that $A_S(R, R_S, d, \theta) = A_S(R, R_S, d, \pi - \theta)$, whereas for $-\pi/2 < \theta < 0$, $A_S(R, R_S, d, \theta) = A_S(R, R_S, d, \theta - \pi)$. In what follows, we solve each of the cases separately.

A.1.1. Case (a)

Before looking at the integrals that lead to the intersection area between the circle and the semi-circle in this case, let us obtain the expressions for the intersection points (a_1, b_1) and (a_2, b_2) . To do this, we first note that the point where the circle intersects with the line $y = 0$ (which is the line that passes through the base of the semi-circle) is given by

$$x_{\text{int}} = -d \cos \theta \pm \sqrt{R^2 - d^2 \sin^2 \theta}. \quad (\text{A1})$$

If the discriminant of this expression is negative (or zero), which in this case implies that $|d \sin \theta| \geq R$, then there is no (or one) intersection of the circle with the x-axis. In this case, the intersectional area can either be zero if $d \geq R + R_S$ or equal to solving the problem of the intersection between two circles of radius R and R_S in the case in which $d < R + R_S$. If the latter case is true, in turn, the intersectional area reduces to πR^2 when $d + R < R_S$ (i.e., when the circle is inside the semi-circle).

If $|d \sin \theta| < R$, then we have two solutions for the intersection points of the circle and the x-axis, x_{int} . The cases in which both solutions are inside the semi-circle, i.e., when $|x_{\text{int}}| \leq R_S$, will be handled in case (c), as depicted in Figure 8. If both solutions are *outside* the semi-circle, i.e., when $|x_{\text{int}}| > R_S$, there are two possibilities. If $d \geq R + R_S$, the intersection area is zero — in this case, the circle is always to the left of the semi-circle. If, on the other hand, $d < R + R_S$, then because the intersections with the x-axis happen outside the semi-circle, there are two options: either the circle intersects twice with the upper part of the semi-circle (a case that will be solved in case (c-2)) or the circle covers all of the semi-circle, in which case the intersectional area is $\pi R_S^2/2$. If $\theta > 0$, then this leaves us, finally, with the problem we will solve for case (a) (is this is not true then case (b) will apply), in which x_{int} has both one solution outside and another one inside the semi-circle. Because here we are dealing with the cases in which the center of the circle is always to the left of the center of the semi-circle, this implies that the intersection point inside the semi-circle will always be the right-most intersection point, i.e., the solution of x_{int} with the positive sign. In the

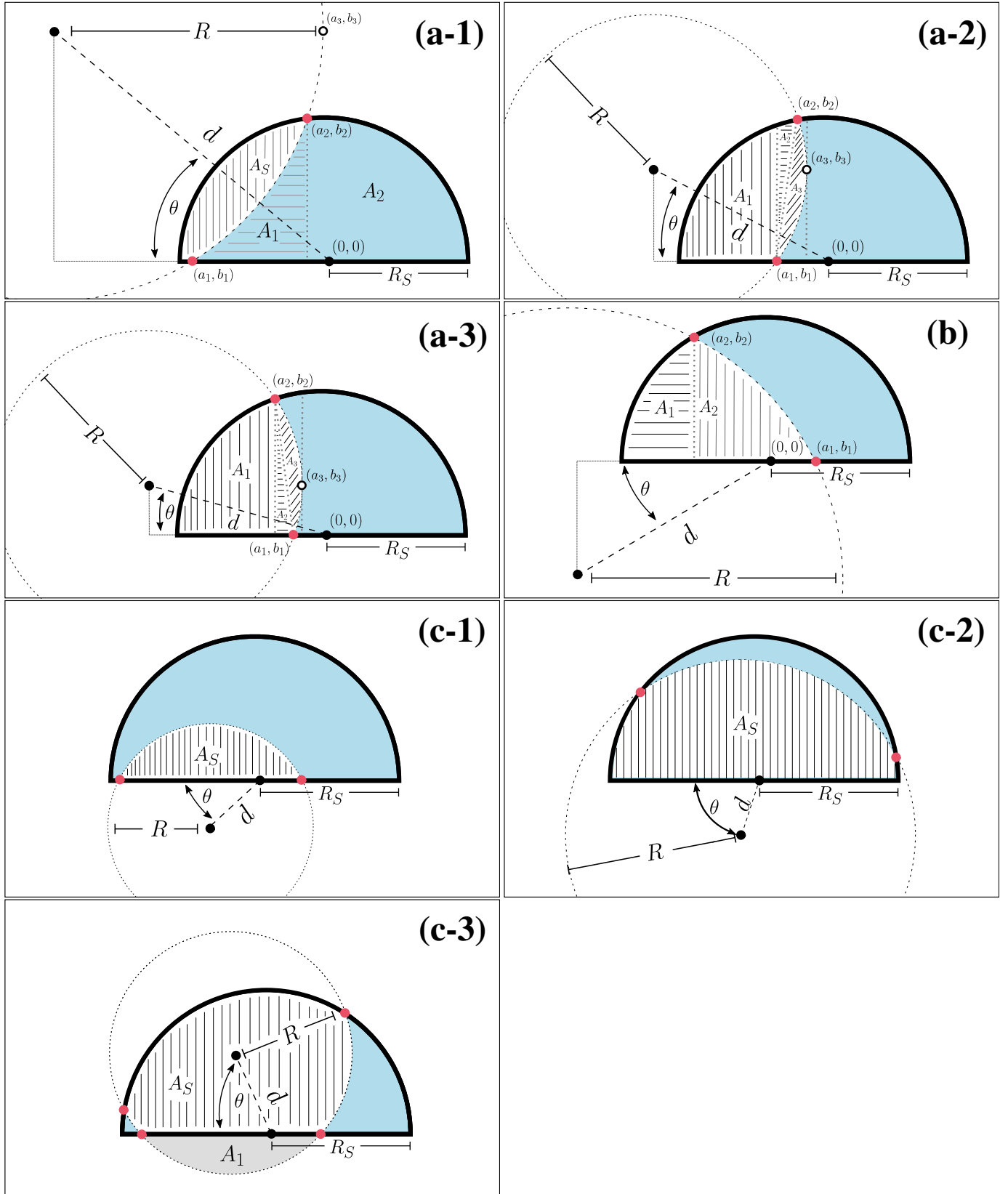


Figure 8. Transformed geometry of the problem — we chose to rotate the circle of radius R around the semi-circle of radius R_S by an angle θ . This problem is the same as having the semi-circle rotated with respect to the line that joins the centers (of length d) by an angle θ . The general problem can, in turn, be divided in three cases: (a) when the center of the circle is above the base of the semi-circle (divided, in turn in sub-cases a-1, a-2 and a-3), (b) when the center of the circle is below the base of the semi-circle and the intersection points are not both touching the base or the edge of the semi-circle and (c) when there are two (c-1) or more (c-2) simultaneous intersection points with either at the edge or at the base of the semi-circle; this latter case can be solved using basic trigonometry. In all cases, the intersection points between the semi-circle and the circle are indicated by red dots. In all cases, the area of interest is the white dashed one inside the semi-circles.

notation of Figure 8, this gives the intersection points

$$\begin{aligned} a_1 &= -d \cos \theta + \sqrt{R^2 - d^2 \sin^2 \theta}, \\ b_1 &= 0. \end{aligned}$$

The intersection point between the upper part of the semi-circle and the circle, (a_2, b_2) , is obtained by simply equating the equation of the circle $((x + d \cos \theta)^2 + (y - d \sin \theta)^2 = R^2)$ with the equation of the semi-circle, taking it as a full circle $(x^2 + y^2 = R_S^2)$ to begin with. This yields

$$b_2 = -A \sin \theta + \cos \theta \sqrt{R_S^2 - A^2}, \quad (\text{A2})$$

$$a_2 = b_2 \tan \theta + \frac{A}{\cos \theta}, \quad (\text{A3})$$

where

$$A = \frac{R^2 - R_S^2 - d^2}{2d}.$$

As we are not dealing with two intersecting circles, but an intersecting circle and semi-circle, we have chosen the largest b_2 which will give rise to the a_2 , and therefore the point of intersection, that is on the semi-circle.

Finally, an important set of coordinates to define are the ones for (a_3, b_3) . As illustrated in Figure 8, these are the coordinates of the maximum value attained in the x-axis by the circle. The coordinates for this point are, evidently,

$$\begin{aligned} a_3 &= -d \cos \theta + R, \\ b_3 &= d \sin \theta. \end{aligned}$$

First, we take on **case (a-1)**. This case occurs when the conditions for case (a) are met and when the point (a_3, b_3) is *outside* the semi-circle, which in turn implies in this case that $b_3 \geq b_2$. To solve it, the strategy to obtain A_S is to compute analytic solutions to the areas A_1 and A_2 depicted in Figure 8, and then subtract these to $\pi R_S^2/2$. First, A_1 is simply the area under the curve of the circle from $x = a_1$ to $x = a_2$. Because in this case $a_1 < a_2 < a_3$, we are going to integrate the lower part of the circle; this implies the equation of the (in this case semi) circle is simply

$$y = -\sqrt{R^2 - (x + d \cos \theta)^2} + d \sin |\theta|.$$

Integrating this from $x = a_1$ to $x = a_2$ yields

$$A_1 = \frac{R^2}{2} \Delta f + d \sin |\theta| (a_2 - a_1), \quad (\text{A4})$$

where $\Delta f = f(a_1) - f(a_2)$, with

$$f(x) = \left(\frac{x + d \cos \theta}{R^2} \right) \sqrt{R^2 - (x + d \cos \theta)^2} + \arcsin \left(\frac{x + d \cos \theta}{R} \right).$$

Next, we work on obtaining area A_2 . This is simply the area under the curve of the semi-circle, whose equation is $y = \sqrt{R_S^2 - x^2}$. Integrating this from $x = a_2$ to $x = R_S$ yields

$$A_2 = \frac{R_S^2}{2} \left[\frac{\pi}{2} - h(a_2) \right], \quad (\text{A5})$$

where

$$h(x) = \arcsin \left(\frac{x}{R_S} \right) + \frac{x}{R_S} \sqrt{1 - \frac{x^2}{R_S^2}}.$$

Thus using the definitions for A_1 given in equation (A4) and for A_2 given in equation (A5), area A_S is given in this case by

$$A_S = \frac{\pi R_S^2}{2} - \frac{R^2}{2} \Delta f - d \sin |\theta| (a_2 - a_1) - \frac{R_S^2}{2} \left[\frac{\pi}{2} - h(a_2) \right].$$

Now, we take on **case (a-2)**. In this case $b_3 < b_2$, however, $a_2 > a_1$. In this case, the area of interest is $A_S = A_1 + A_2 + A_3$, as depicted in Figure 8. First, area A_1 in this case is the area of the semi-circle from $x = -R_S$ to $x = a_1$. Integrating once again the equation of the semi-circle ($y = \sqrt{R_S^2 - x^2}$) in this range one obtains

$$A_1 = \frac{R_S^2}{2} \left[h(a_1) + \frac{\pi}{2} \right]. \quad (\text{A6})$$

Area A_2 in this case can be calculated as the area under the same semi-circle between $x = a_1$ and $x = a_2$ *minus* $b_2(a_2 - a_1)/2$, which is the area of the triangle formed between the points (a_1, b_1) , (a_2, b_2) and $(a_2, 0)$. Integrating the semi-circle between $x = a_1$ and $x = a_2$ and subtracting $b_2(a_2 - a_1)/2$, we obtain

$$A_2 = \frac{R_S^2}{2} [h(a_2) - h(a_1)] - \frac{b_2(a_2 - a_1)}{2}. \quad (\text{A7})$$

Finally, area A_3 reduces to obtaining the segment of a circle generated by drawing a chord between points (a_1, b_1) and (a_2, b_2) . To this end, we ought to know the angle α (in radians) these points make with respect to the center of the circle. This can be easily obtained by the Law of Cosines to give

$$\alpha = \arccos \left(1 - \frac{(a_2 - a_1)^2 + b_2^2}{2R^2} \right).$$

With this, the area of the segment A_3 is thus, simply

$$A_3 = \frac{R^2}{2} (\alpha - \sin \alpha). \quad (\text{A8})$$

Finally, then, using the definition for A_1 in equation (A6), for A_2 in equation (A7) and for A_3 in equation (A8), we get in this case

$$A_S = \frac{R_S^2}{2} \left[h(a_2) + \frac{\pi}{2} \right] - \frac{b_2(a_2 - a_1)}{2} + \frac{R^2}{2} (\alpha - \sin \alpha).$$

Finally, we solve **case (a-3)**. In this case again $b_3 < b_2$, however, $a_1 > a_2$. Here, equation (A6) also applies for A_1 , but the upper limit of the integral is in this case a_2 instead of a_1 . This implies that in this case

$$A_1 = \frac{R_S^2}{2} \left[h(a_2) + \frac{\pi}{2} \right]. \quad (\text{A9})$$

To obtain area A_2 in this case, we note that here this is simply the area of the triangle formed by the points with coordinates (a_1, b_1) , (a_2, b_2) and $(a_2, 0)$. In this case, thus,

$$A_2 = \frac{b_2(a_1 - a_2)}{2}. \quad (\text{A10})$$

Finally, to obtain A_3 we use equation (A8) which also applies for this case. Using then the definition for A_1 in equation (A9), for A_2 in equation (A10) and for A_3 in equation (A8), we get in this case

$$A_S = \frac{R_S^2}{2} \left[h(a_2) + \frac{\pi}{2} \right] + \frac{b_2(a_1 - a_2)}{2} + \frac{R^2}{2} (\alpha - \sin \alpha).$$

A.1.2. Case (b)

Case (b) is similar in many ways to case (a), with the only difference that now the coordinates of the center of the circle change to $(-d \cos \theta, -d \sin |\theta|)$, and thus some functions and integration ranges change signs. In this case, the intersection points of the circle with the x-axis are the same as the ones given in equation (A1), and thus all of the discussion given at the beginning of the past sub-section also applies for case (b). In particular, the intersection points (a_1, b_1) and (a_2, b_2) derived for case (a) are the same for this case.

In this case, the area of interest is the sum of area A_1 and A_2 . The former is the integral of the semi-circle circle from $x = -R_S$ to $x = a_2$, which is an integral which was already found in equation (A9). As for area A_2 , this is the integral of the upper part of the circle of radius R , i.e., of the function

$$y = \sqrt{R^2 - (x + d \cos \theta)^2} - d \sin |\theta|.$$

However, the integral of this from $x = a_2$ to $x = a_1$ is exactly the same integral calculated in case (a-1), whose result is on equation (A4), because the integrand there was the same integrand that we have here but multiplied by -1, and the limits of integration there were reversed with respect to the ones we have here (i.e., they went from a_1 to a_2) — because inverting the limits of integration is the same as calculating the integral multiplied by -1, both effects cancel out. Thus, area A_2 in our case is area A_1 in case (a-1). Thus, for case (b), we have that $A_S = A_1 + A_2$, i.e.,

$$A_S = \frac{R_S^2}{2} \left[h(a_2) + \frac{\pi}{2} \right] + \frac{R^2}{2} \Delta f + d \sin |\theta| (a_2 - a_1).$$

A.1.3. Case (c)

Case (c) focuses on when $|d \sin \theta| < R$, i.e. there are two solutions for the intersection points of the circle with the line $y = 0$.

More specifically, **case (c-1)** occurs also when $|x_{\text{int}}| \leq R_S$, i.e. when the two solutions for the intersection points are inside the semi-circle and when the part of the circle above the intersection points is completely enclosed within the semi-circle (see Figure 8). This can be quantitatively described by theoretically ‘extending’ the semi-circle into a full circle of radius R_S . The coordinates of intersection of these two circles (setting the center of the circle of radius R_S at the origin) can be found by substituting $x^2 + y^2 = R_S^2$ into $(x + d \cos \theta)^2 + (y + d \sin \theta)^2 = R^2$ to give the y coordinates:

$$y = -A \sin \theta \pm \cos \theta \sqrt{R_S^2 - A^2},$$

where

$$A = \frac{R^2 - R_S^2 - d^2}{2d}.$$

This is similar to equations A2 and A3 except the position of the circles relative to the origin have been changed slightly.

Therefore case (c-1) applies when $|x_{\text{int}}| \leq R_S$ and either:

- There is no solution for the intersection of the two circles. This will occur when $A^2 > R_S^2$.
- Both of the y-coordinate solutions are real and negative, i.e. when $-A \sin \theta \pm \cos \theta \sqrt{R_S^2 - A^2} < 0$.

Case (c-2) occurs when $|x_{\text{int}}| > R_S$ and when there are two intersection points on the curved edge of the semi-circle. For this case, the y-coordinates of intersection between the circle R and the full circle of radius R_S must be positive. Using the same equations as above, this is when $-A \sin \theta \pm \cos \theta \sqrt{R_S^2 - A^2} \geq 0$, where A is defined as in case (c-1).

Case (c-3) occurs when $|x_{\text{int}}| \leq R_S$ and when there are two further intersection points on the curved edge of the semi-circle, making a total of four intersections points. Therefore case (c-3) is when $|x_{\text{int}}| \leq R_S$ and $-A \sin \theta \pm \cos \theta \sqrt{R_S^2 - A^2} \geq 0$.

To solve case (c-1), the points of intersection in the base of the semi-circle can be obtained via equation A1:

$$x_{\text{int}}^{\pm} = -d \cos \theta \pm \sqrt{R^2 - d^2 \sin^2 \theta}.$$

The problem is then just calculating the area of the segment A_S which is a well-known geometric problem with the solution

$$A_S = R^2 \arccos \left(\frac{y}{R} \right) - xy,$$

where

$$\begin{aligned} x &= (1/2)(x_{\text{int}}^+ + |x_{\text{int}}^-|), \\ &= \sqrt{R^2 - d^2 \sin^2 \theta}, \\ y &= -d \sin \theta. \end{aligned}$$

To solve case (c-2), the problem can be set up by first theoretically 'extending' the semi-circle into a full circle of radius R_S and calculating the area of intersection of the two circles using the equations described in Kreidberg (2015):

$$A_{\text{int}} = R^2 \arccos u + R_S^2 \arccos v - (1/2)\sqrt{w}, \quad (\text{A11})$$

where

$$\begin{aligned} u &= (d^2 + R^2 - R_S^2)/(2dR), \\ v &= (d^2 + R_S^2 - R^2)/(2dR_S), \\ w &= (-d + R + R_S)(d + R - R_S)(d - R + R_S)(d + R + R_S). \end{aligned}$$

Using A_{int} , one can find A_S by subtracting half the area of the 'extended' circle of radius R_S to yield

$$A_S = A_{\text{int}} - \pi R_S^2/2.$$

To solve case (c-3), the problem needs to be split up into two parts. The first part involves finding the area of intersection, A_{int} , of the circle and the semi-circle 'extended' into a full circle of radius R using the same method from part (c-2) and the second involves finding area A_1 . As can be seen from the Figure 8, once these two areas are found, it is simply a matter of subtracting A_1 from A_{int} to find A_S .

To find A_1 is a very similar problem to case (c-1), the points of intersection along the base of the semi-circle can be found using equation A1 and then the problem reduces to that of finding the area of a segment, which is A_1 in this case. Following a similar method for case (c-1),

$$A_1 = R^2 \arccos \left(\frac{-y}{R} \right) + xy,$$

where x and y are defined the same as for case (c-1), however note change in sign of y , due to the change of orientation of the shapes. As mentioned, A_{int} is the same as in case (c-2) and is described in equation A11.

Therefore the total intersection area A_S , is given by

$$A_S = A_{\text{int}} - A_1$$

A.2. Deriving θ

In this paper we have defined θ as the angle between the base of the semi-circle and the line that extends from the base of the semi-circle to the center of the circle (of length d). Importantly, θ is defined as *positive* when extending clockwise, assuming the center of the circle is to the left of the semi-circle which, as explained in section A.1, due to the symmetry of the problem, can always be achieved by flipping the frame of reference.

θ is calculated from parameters that correspond to how the system physically appears in the sky. Due to the symmetry of the star, the planet is assumed to move horizontally across it, without loss of generality, along an axis that will be referred to as the 'original horizontal axis', differentiating it from the $y = 0$ axis used in section A.1 when the frame is rotated so that the base of the semi-circle is at the origin and the base lies along this axis. θ therefore depends on the angle the semi-circle is rotated through with respect to the original horizontal axis, ϕ , the impact parameter, b and whether the semi-circle is originally to the left or the right of the center of the circle. The latter is characterised by the time, t and the time of inferior conjunction, t_0 .

ϕ is defined in this paper between the range $-\pi/2$ to $\pi/2$, from the original horizontal axis to the base of the *top* semi-circle, where a positive angle is defined going in the anticlockwise direction. Once this is used to find the θ for $R_{p,1}$, to obtain the θ for $R_{p,2}$, one simply has to multiply θ by -1, due to the change in direction.

Table A.2 shows how θ is calculated for the different values of ϕ , b and t for $R_{p,1}$.

t	b	ϕ	θ
$\leq t_0$	positive	$< \arccos b/d$	$-\phi - \arcsin b/d$
		$\geq \arccos b/d$	$-\pi + \phi + \arcsin b/d$
$\leq t_0$	negative	$\leq -\arccos b /d$	$\pi + \phi - \arcsin b /d$
		$> -\arccos b /d$	$-\phi + \arcsin b /d$
$> t_0$	positive	$< -\arccos b/d$	$-\pi - \phi + \arcsin b/d$
		$\geq -\arccos b/d$	$\phi - \arcsin b/d$
$> t_0$	negative	$\leq \arccos b /d$	$\phi + \arcsin b /d$
		$> \arccos b /d$	$\pi - \phi - \arcsin b /d$

A.3. Change in ϕ and the y -coordinate of the semi-circle due to orbital mechanics

If the planet were to move in a straight line across the star, then the planet's y -coordinate would stay constant at the value of the impact parameter, b . From Seager (2010) this is defined as

$$b = \frac{a \cos i}{R_{\text{star}}} \left(\frac{1 - e^2}{1 - e \sin \varpi} \right), \quad (\text{A12})$$

where a is the semi-major axis, i is the inclination of the orbit, e is the eccentricity, ϖ is the longitude of periastron and R_{star} is the radius of the star. However due to the orbital motion of the planet around the star, the y -coordinate of the planet changes slightly. For the most accurate model, b used in the equations in A.2 should be adjusted to

$$b = -r \sin(\omega + f) \cos i, \quad (\text{A13})$$

where

$$r = \frac{a(1 - e^2)}{1 + e \cos f}, \quad (\text{A14})$$

$$\cos f = \frac{\cos E - e}{1 - e \cos E}, \quad (\text{A15})$$

$$E - e \sin E = \frac{2\pi}{T}(t - t_0). \quad (\text{A16})$$

T is the orbital period of the planet, t is the current time of interest and t_0 is the time of periastron passage. The last equation can be solved numerically using a Newton-Raphson method.

Furthermore, due to the change in gradient of the planet's orbit with respect to Earth, the angle ϕ of the semi-circle will change slightly as it passes across the circle. The change in angle caused by this movement will be labelled ψ and should be added to the original ϕ . To derive ψ and make it clearer, b has been re-labelled to y . By differentiating,

$$dy = -r \cos(\varpi + f) \cos i \, df. \quad (\text{A17})$$

Also explained in Seager (2010), the x -coordinate of the center of the semi-circle will move as

$$x = -r \cos(\varpi + f), \quad (\text{A18})$$

and so

$$dx = -r \sin(\varpi + f) \, df. \quad (\text{A19})$$

Therefore ψ can be calculated from

$$\tan \psi = \frac{dy}{dx}, \quad (\text{A20})$$

$$\psi = \arctan[\cot(\varpi + f) \cos i]. \quad (\text{A21})$$

Then, ϕ should be adjusted so that

$$\phi_{\text{new}} = \phi_{\text{old}} + \psi \quad (\text{A22})$$

Software: NumPy (Harris et al. 2020), Scipy (Virtanen et al. 2020), Matplotlib (Hunter 2007), batman (Kreidberg et al. 2015), juliet (Espinoza et al. 2019), catwoman (Jones & Espinoza 2020).

REFERENCES

- Ahlers, J. P., Johnson, M. C., Stassun, K. G., et al. 2020, *AJ*, 160, 4, doi: [10.3847/1538-3881/ab8fa3](https://doi.org/10.3847/1538-3881/ab8fa3)
- Batalha, N. E., Mandell, A., Pontoppidan, K., et al. 2017, *PASP*, 129, 064501, doi: [10.1088/1538-3873/aa65b0](https://doi.org/10.1088/1538-3873/aa65b0)
- Buchner, J., Georgakakis, A., Nandra, K., et al. 2014, *A&A*, 564, A125, doi: [10.1051/0004-6361/201322971](https://doi.org/10.1051/0004-6361/201322971)
- Burrows, A., Sudarsky, D., & Hubbard, W. B. 2003, *ApJ*, 594, 545, doi: [10.1086/376897](https://doi.org/10.1086/376897)
- Charbonneau, D., Brown, T. M., Latham, D. W., & Mayor, M. 2000, *ApJL*, 529, L45, doi: [10.1086/312457](https://doi.org/10.1086/312457)
- Espinoza, N., Fortney, J. J., Miguel, Y., Thorngren, D., & Murray-Clay, R. 2017, *ApJL*, 838, L9, doi: [10.3847/2041-8213/aa65ca](https://doi.org/10.3847/2041-8213/aa65ca)
- Espinoza, N., Kossakowski, D., & Brahm, R. 2019, *MNRAS*, 490, 2262, doi: [10.1093/mnras/stz2688](https://doi.org/10.1093/mnras/stz2688)
- Feroz, F., Hobson, M. P., & Bridges, M. 2009, *MNRAS*, 398, 1601, doi: [10.1111/j.1365-2966.2009.14548.x](https://doi.org/10.1111/j.1365-2966.2009.14548.x)
- Fortney, J. J. 2005, *MNRAS*, 364, 649, doi: [10.1111/j.1365-2966.2005.09587.x](https://doi.org/10.1111/j.1365-2966.2005.09587.x)
- Goyal, J. M., Mayne, N., Sing, D. K., et al. 2018, *MNRAS*, 474, 5158, doi: [10.1093/mnras/stx3015](https://doi.org/10.1093/mnras/stx3015)
- Greene, T. P., Line, M. R., Montero, C., et al. 2016, *ApJ*, 817, 17, doi: [10.3847/0004-637X/817/1/17](https://doi.org/10.3847/0004-637X/817/1/17)
- Harris, C. R., Millman, K. J., van der Walt, S. J., et al. 2020, *Nature*, 585, 357, doi: [10.1038/s41586-020-2649-2](https://doi.org/10.1038/s41586-020-2649-2)
- Helling, C., Kawashima, Y., Graham, V., et al. 2020, *A&A*, 641, A178, doi: [10.1051/0004-6361/202037633](https://doi.org/10.1051/0004-6361/202037633)
- Henry, G. W., Marcy, G. W., Butler, R. P., & Vogt, S. S. 2000, *ApJL*, 529, L41, doi: [10.1086/312458](https://doi.org/10.1086/312458)
- Hubbard, W. B., Fortney, J. J., Lunine, J. I., et al. 2001, *ApJ*, 560, 413, doi: [10.1086/322490](https://doi.org/10.1086/322490)
- Hunter, J. D. 2007, *Computing in Science & Engineering*, 9, 90, doi: [10.1109/MCSE.2007.55](https://doi.org/10.1109/MCSE.2007.55)
- Jones, K., & Espinoza, N. 2020, *Journal of Open Source Software*, 5, 2382, doi: [10.21105/joss.02382](https://doi.org/10.21105/joss.02382)
- Kempton, E. M. R., Bean, J. L., & Parmentier, V. 2017, *ApJL*, 845, L20, doi: [10.3847/2041-8213/aa84ac](https://doi.org/10.3847/2041-8213/aa84ac)
- Kipping, D. M. 2013, *MNRAS*, 435, 2152, doi: [10.1093/mnras/stt1435](https://doi.org/10.1093/mnras/stt1435)
- Kreidberg, L. 2015, *PASP*, 127, 1161, doi: [10.1086/683602](https://doi.org/10.1086/683602)
- . 2018, *Exoplanet Atmosphere Measurements from Transmission Spectroscopy and Other Planet Star Combined Light Observations*, 100, doi: [10.1007/978-3-319-55333-7_100](https://doi.org/10.1007/978-3-319-55333-7_100)
- Kreidberg, L., Line, M. R., Bean, J. L., et al. 2015, *ApJ*, 814, 66, doi: [10.1088/0004-637X/814/1/66](https://doi.org/10.1088/0004-637X/814/1/66)
- Line, M. R., & Parmentier, V. 2016, *ApJ*, 820, 78, doi: [10.3847/0004-637X/820/1/78](https://doi.org/10.3847/0004-637X/820/1/78)
- MacDonald, R. J., Goyal, J. M., & Lewis, N. K. 2020, *ApJL*, 893, L43, doi: [10.3847/2041-8213/ab8238](https://doi.org/10.3847/2041-8213/ab8238)
- Mordasini, C., van Boekel, R., Mollière, P., Henning, T., & Benneke, B. 2016, *ApJ*, 832, 41, doi: [10.3847/0004-637X/832/1/41](https://doi.org/10.3847/0004-637X/832/1/41)
- Nikolov, N., & Sainsbury-Martinez, F. 2015, *ApJ*, 808, 57, doi: [10.1088/0004-637X/808/1/57](https://doi.org/10.1088/0004-637X/808/1/57)
- Öberg, K. I., Murray-Clay, R., & Bergin, E. A. 2011, *ApJL*, 743, L16, doi: [10.1088/2041-8205/743/1/L16](https://doi.org/10.1088/2041-8205/743/1/L16)
- Parmentier, V., Showman, A. P., & Fortney, J. J. 2020, *arXiv e-prints*, arXiv:2010.06934, <https://arxiv.org/abs/2010.06934>
- Pontoppidan, K. M., Pickering, T. E., Laidler, V. G., et al. 2016, *Society of Photo-Optical Instrumentation Engineers (SPIE) Conference Series*, Vol. 9910, Pandeia: a multi-mission exposure time calculator for JWST and WFIRST, 991016, doi: [10.1117/12.2231768](https://doi.org/10.1117/12.2231768)
- Powell, D., Loudén, T., Kreidberg, L., et al. 2019, *arXiv e-prints*, arXiv:1910.07527, <https://arxiv.org/abs/1910.07527>
- Rauscher, E., Menou, K., Seager, S., et al. 2007, *ApJ*, 664, 1199, doi: [10.1086/519213](https://doi.org/10.1086/519213)
- Rein, E., & Ofir, A. 2019, *MNRAS*, 490, 1111, doi: [10.1093/mnras/stz2556](https://doi.org/10.1093/mnras/stz2556)
- Ricker, G. R., Winn, J. N., Vanderspek, R., et al. 2014, *Society of Photo-Optical Instrumentation Engineers (SPIE) Conference Series*, Vol. 9143, Transiting Exoplanet Survey Satellite (TESS), 914320, doi: [10.1117/12.2063489](https://doi.org/10.1117/12.2063489)
- Roman, M., & Rauscher, E. 2019, *ApJ*, 872, 1, doi: [10.3847/1538-4357/aafdb5](https://doi.org/10.3847/1538-4357/aafdb5)
- Schwarz, G. 1978, *Ann. Statist.*, 6, 461, doi: [10.1214/aos/1176344136](https://doi.org/10.1214/aos/1176344136)
- Seager, S. 2010, *Exoplanets*
- Seager, S., & Sasselov, D. D. 2000, *ApJ*, 537, 916, doi: [10.1086/309088](https://doi.org/10.1086/309088)
- Sheppard, K. B., Welbanks, L., Mandell, A., et al. 2020, *arXiv e-prints*, arXiv:2010.09659, <https://arxiv.org/abs/2010.09659>
- Sing, D. K., Fortney, J. J., Nikolov, N., et al. 2016, *Nature*, 529, 59, doi: [10.1038/nature16068](https://doi.org/10.1038/nature16068)

- Virtanen, P., Gommers, R., Oliphant, T. E., et al. 2020, Nature Methods
- von Paris, P., Gratier, P., Bordé, P., Leconte, J., & Selsis, F. 2016, A&A, 589, A52, doi: [10.1051/0004-6361/201527894](https://doi.org/10.1051/0004-6361/201527894)
- Wakeford, H. R., Sing, D. K., Stevenson, K. B., et al. 2020, AJ, 159, 204, doi: [10.3847/1538-3881/ab7b78](https://doi.org/10.3847/1538-3881/ab7b78)
- Welbanks, L., Madhusudhan, N., Allard, N. F., et al. 2019, ApJL, 887, L20, doi: [10.3847/2041-8213/ab5a89](https://doi.org/10.3847/2041-8213/ab5a89)
- Williams, P. K. G., Charbonneau, D., Cooper, C. S., Showman, A. P., & Fortney, J. J. 2006, ApJ, 649, 1020, doi: [10.1086/506468](https://doi.org/10.1086/506468)